Chapter 5

Motion Artifact Suppression for In-plane Rigid Rotation

5.1 Introduction

An improved algorithm based on the bilinear superposition algorithm (BSA) [78], for planar rotational motion artifact suppression in standard 2D Fourier transform magnetic resonance images is presented in this chapter. It is shown in the previous chapter, that interpolation of acquired view data on the uncorrupted k-space create data overlap and void regions. A method of managing overlapping data regions is presented in this chapter, using weighted averaging of redundant data. The weights are assigned according to a priority ranking based on the minimum distance between the data set and the k-space grid points. An iterative estimation technique for filling the data void regions, using projection onto convex sets (POCS), is also described.

Several publications have proposed methods of reducing rotational motion artifacts within the imaging plane [7][78][80]-[82]. However, most of these methods

are limited to the suppression of small angle rotational motion artifacts. In this chapter, an improved method capable of suppressing motion artifacts due to large angle rotations of the imaged object is presented. Only gross rotations in the imaging plane are considered. The movement is assumed to be sufficiently slow, that the imaged object is considered to be stationary during the acquisition of a single view of data. Hence, the motion is an inter-view effect, a condition which is generally satisfied in the case of gross movement [62]. The rotation angles at the acquisition of each view are considered known, using navigator echo information or using post-processing techniques, such as the method described in Chapter 4.

5.2 Bilinear Superposition Algorithm (BSA)

One of the popular data correction methods in MRI, is to use bilinear interpolation in the spatial domain followed by superposition on to the corrected k-space [78]. In this method, the MRI spatial frequency components are assumed to be the superposition of N different images corresponding to N different phase encoding steps. In each of the N images, only one line, corresponding to the phase encoding step, is non-zero and the other lines are zero. It is assumed that the zero lines have the motional parameters of the non-zero line. Hence the planar rigid motion parameters are fixed for all lines of each of the N different images. Alternatively, using the superposition property, the inverse 2-DFT of the MR signal can be obtained by adding the inverse 2-DFT of the previously discussed N images. Using the k-space data, the reconstruction algorithm is described as follows:

- Step 1) Correct the phase error of the k-space data using the translational motion parameters, which are assumed to be known or have been estimated using post-processing techniques [59][61][65][69].

- Step 2) Divide the k-space data into N different images so that each image contains one non-zero line, and the other lines are filled with zeros.
- Step 3) Calculate the inverse 2-DFT of the N-different images.
- Step 4) Using the bilinear interpolation method, back-rotate each of the N different images by its estimated rotation angle corresponding to the phase encoding step of the non-zero line. Rotation angle estimation can be performed using the method described in Chapter 4.
- Step 5) Calculate the 2-DFT of the N different images.
- Step 6) To obtain the corrected MR signal, the 2-DFT values of step 5 can be superimposed on a new k-space.
- Step 7) Calculate the inverse 2-DFT of the new k-space.

Figure 5.1 illustrates these steps involved in BSA, in a graphical point of view, with respect to corrected (i.e. new) and un-corrected (i.e. original) k-spaces. In the early versions of BSA [136], the 2-DFT of the sum of the images had been applied instead of steps 5 and 6. However, it caused the leakage spatial frequency components due to interpolation, to overlap with each other, thereby degrading the quality of the resultant MR image. Although the introduction of steps 5 and 6 eliminate this problem, it does not address the general problem of overlap data and data void regions as described in Section 4.2, and later in Section 5.3. Since the above algorithm interpolates data on one line of the k-space using only the rotated version of the same line of the k-space data, it gives accurate results only around the region where the lines intersect, restricting the algorithm to be effective only for small angle rotations. This problem is addressed in detail in the Section 5.4.

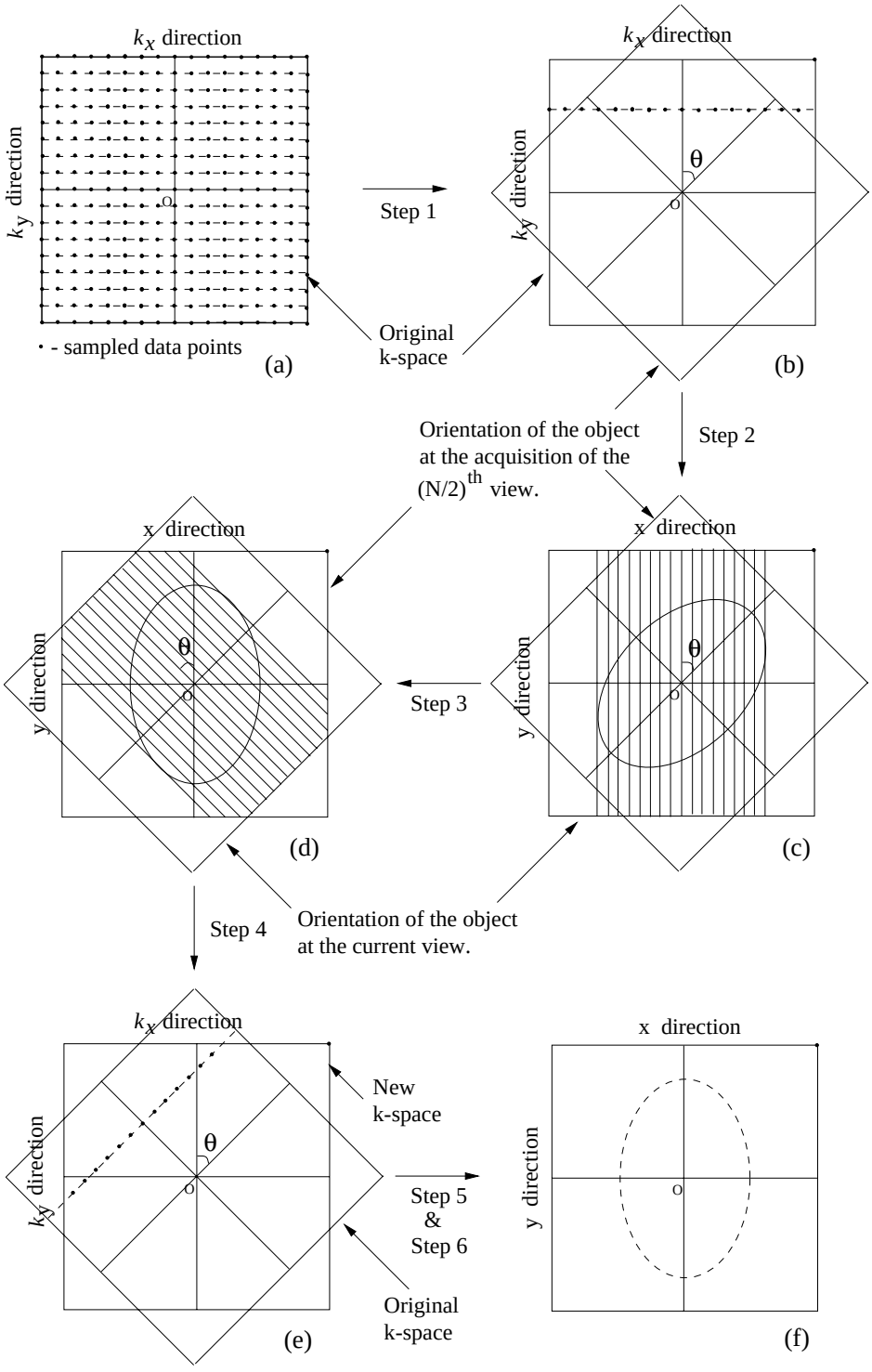

Figure 5.1: Graphical illustration of BSA: *(a)* acquired motion affected k-space data; *(b)* One of N different views selected as the non-zero line; *(c)* result of inverse 2-DFT on the selected view; *(d)* rotation correction using bilinear interpolation; *(e)* result obtained by performing 2-DFT on the interpolated spatial domain; *(f)* final image reconstructed from calculating 2-DFT of the superimposed k-space data from all the N views.

The steps 1 through to 5 of BSA are involved in the resampling of the k-space non-uniform sampled data. However, the interpolation has been performed in the spatial domain. Therefore, the interpolation errors resulting from the high variance of k-space data have been avoided. To increase the speed of the algorithm, in step 2, instead of computing the inverse 2-DFT, inverse 1-DFT of the non-zero line along the k_x direction can be computed prior to calculating the inverse 1-DFT of all the lines along the k_y direction. As there is only one non-zero value at each line along the k_y direction, the inverse 1-DFT can be obtained very rapidly.

Since step 3 of the algorithm must be repeated N times, the selected interpolation method has to be fast as well as accurate. The bilinear interpolation technique is ideal for this purpose due to its speed and low variance of the intensity distribution of the images in the spatial domain.

5.3 Data Overlap and Void Regions

As described in Section 4.2, data overlapping can occur between any number of different views, rotated at different angles, hence producing significant regions of data overlap. Only $N \times N$ data samples are acquired from all the N views, and there are $N \times N$ grid points required to be filled in the uncorrupted k-space. Therefore, if some of the grid points are over-represented due to data overlap, it is logical to expect some grid points to be under-represented due to data voids.

5.4 Management of Overlap Data

At a data overlap, the interpolation errors associated with each data sample can differ considerably. Therefore, in practice, the overlapping samples at a

particular grid point can be ranked according to their interpolation accuracy. Such a system of ranking enables the assigning of weights to each sample, prior to computing the average spatial frequency value at a particular grid point in the corrected k-space. Weighted averaging of redundant data can also lead to improved performance under noisy conditions.

In bilinear superposition algorithm [78], the interpolation was performed in the spatial domain, which reduced the interpolation errors caused by high variance in the spatial frequency data. However, the fact that each of the interpolations is performed using only a single view of data at a time, cannot be discounted. Effectively, the attempt is to interpolate values on to a 2D grid using 1D signal data spanning on an inclined line on the 2D k-space. The adjacent grid points to this inclined line are filled using interpolated values as shown in Figure 5.2(a). Obviously, the more the deviation (d) of the grid point from the inclined line, the less accurate the interpolated value will be.

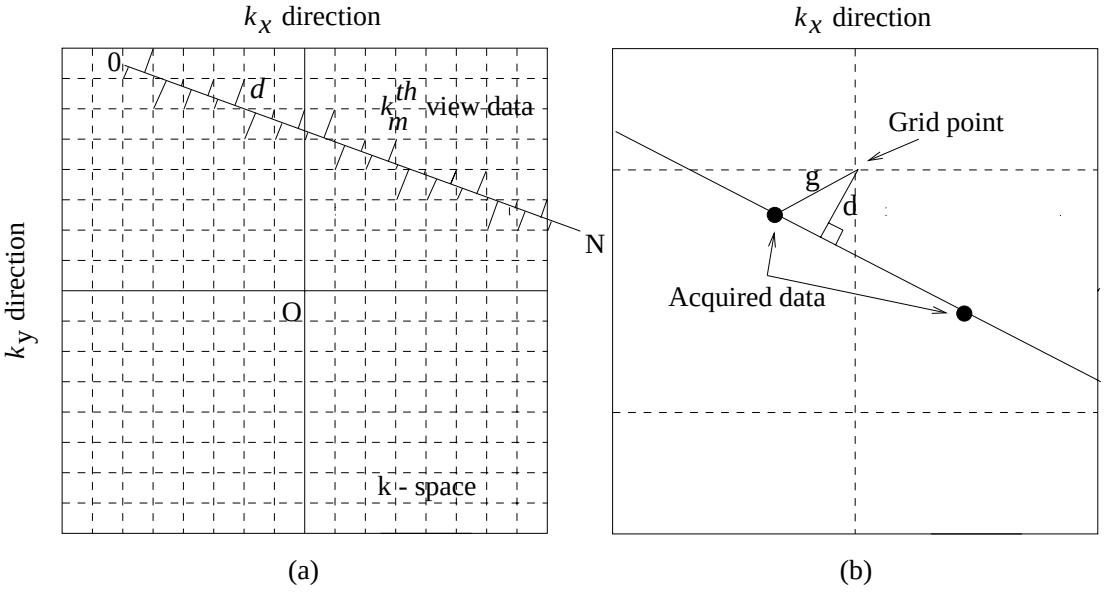

Figure 5.2: *(a)* Deviation between the acquired view data and the required grid points; *(b)* Graphical representation of the distance "d".

Notice that "d" is not the offset distance between the nearest data sample and the grid point which is represented by "g" in Figure 5.2(b). Since acquired

data is available along an inclined line, the interpolation error associated along the direction of this line is significantly lower compared to the interpolation error associated with the direction perpendicular to it. Along this perpendicular direction, there are no data available. Therefore, the ranking is based on the distance "d" between the prospective grid point and the nearest view, which is given by

$$d = |k_{yo} \cos\theta_r(k_m) + k_{xo} \sin\theta_r(k_m) - k_m| \tag{5.1}$$

where (k_{xo}, k_{yo}) are the coordinates of the grid point, $\theta_r(k_m)$ is the rotation angle and k_m is the phase encoded view number.

Therefore, the weight w_r related to the r^{th} sample S_r in an overlap region can be assigned as follows:

$$w_r = \frac{1}{d_r} \tag{5.2}$$

The corrected spatial frequency value $S(k_x, k_y)$ at (k_x, k_y) grid point in the k-space can be computed using;

$$S(k_x, k_y) = \frac{\sum_{r=1}^{m} w_r S_r}{\sum_{r=1}^{m} w_r} \tag{5.3}$$

where m is the total number of competing samples.

A minor modification is incorporated in order to include the reliability of the estimated rotation angles (i.e. $\mu[\theta_{est}(k_m)]$ of Chapter 4). At the reconstruction stage, weights at the data overlap points are decided not only on the distance "d" between the prospective grid point in the k-space and the nearest view, but also on the value of $\mu[\theta_{est}(k_m)]$. Since the value of "d" may vary within the interval $[0, 1]$, with the highest weight at 0 and the lowest at 1, the value of "d" is mapped to a membership function as shown in Equation 5.4;

$$\mu(d) = \frac{1}{1 + ad^2} \tag{5.4}$$

where the constant a is set arbitrarily to 16 for all cases involved in this study. Since both $\mu(d)$ and $\mu[\theta_{est}(k_m)]$ represent fuzzy sets [131], the weights (w) are

decided based upon the fuzzy intersection of these sets, as given below:

$$w = \mu(d) \wedge \mu\left[\theta_{est}\left(k_m\right)\right] \tag{5.5}$$

where $\wedge$ represents the fuzzy intersection [131]. In this work, *minimum* operation is used for fuzzy intersection. However, other t-norms such as bounded difference, Einstein product, algebraic product or Hamacher product [115] can equally well be used. The decision to use *minimum* is based on the fact that it gives the largest w value out of the possible t-norms mentioned above.

The algorithm to manage data overlap can be formulated as follows:

1. Divide the acquired views in to p different groups, each containing a set of views subjected to rotations at the same angle. Grouping such views together not only reduces interpolation errors but also decreases the reconstruction time. If there are p such groups (i.e. $p \leq N$), only p transformations to the spatial domain are required, instead of N, to perform interpolations. If the motion is continuous, then $p = N$.

2. Insert each group into a zeroed $N \times N$ complex matrix.

3. Calculate the inverse 2DFT of the p different matrices.

4. Using bilinear interpolation, back-rotate each of the p different images by the known rotation angle.

5. Calculate the 2DFT of the p different images.

6. Compute the "d" values corresponding to each sample.

7. If a particular grid point does not have a view within "d" value of unity, such a grid point is masked and set to zero. This step is included to eliminate any leakage spatial frequency components, generated due to interpolation in the spatial domain. The resulting spatial frequency values are at most one unit away from the acquired view which spans an inclined line.

8. Calculate the weights (w) associated with each corrected k-space value, incorporating the membership values $\mu(d)$ and $\mu\left[\theta_{est}\left(k_m\right)\right]$.

9. Compute the weighted average values at each k-space grid point.

5.5 Iterative Estimation of Missing Data

Although reconstructed image quality can be partly enhanced by weighted averaging of redundant data, the data void regions in the corrected k-space may still degrade the final image quality, by way of reduced intensity at particular regions and blurred edges caused by the non-availability of particular spatial frequency components.

An analytical method using the Least Squares Error (LSE) technique to estimate low spatial frequency values was proposed by Yan et al. [132]. This method is limited to estimating very small number of missing data, where the number of unknowns is much smaller than the number of equations in the LSE problem. However, when the number of required estimations increases, the problem becomes ill-posed and the estimation is observed to be noise sensitive and computationally unstable.

Since the rotations at large angles produce large data void regions, the estimation technique is required to be capable of estimating in excess of 10,000 samples for a 256×256 image. Therefore, the analytical method [132] is ineffective due to the ill-posedness and prohibitive computational complexity.

The problem of estimating missing spatial frequency values is often encountered in Computed Tomography (CT) [100][133]-[135], and in confocal scanning microscopy [93]. This problem is named the "missing cone problem" and several

methods have been proposed, to suppress the artifacts in the reconstructed image. However, there is some problem-specific information regarding the missing cone problem, which is not valid for the frequency estimation problem described in this section. The non-iterative solutions to the missing cone problem, that range from the two dimensional extrapolation in the Fourier domain [133] to the multicoset sampling approach [134], all use problem-specific information such as;

1. missing spatial frequencies are restricted to a cone shaped region and,
2. the complete sinograms of acquired data posses bow-tie shaped spectral support.

The proposed iterative techniques mostly use projections on to convex sets (POCS) as the basis of the algorithm [100]. A technique using artificial neural network (ANN) has been proposed [135]. However, the neural network structure is dependent upon the problem specific information, which inhibits its application to a general problem such as the one introduced in this section.

Considering the arbitrary shape of the data missing regions and the available *a priori* information on the imaged object, the method of POCS was found to be an effective and efficient technique to estimate a large number of missing spatial frequency values.

A detailed review of POCS is included in Chapter 1. It should be noted that any solution in the intersection set C_o is consistent with the given constraints and therefore a feasible solution. In general, there are many feasible solutions if C_o contains more than a single point in the Hilbert space. It can also be shown that different initial estimates may lead to different solutions.

The following sets and their corresponding projection operators are used to estimate the missing spatial frequency components:

(1) Finite support constraint: The image has a finite region of interest (ROI) bounded by the outer boundary of the imaged object. Therefore, ROI is everything but the background of the image. Each iteration of the algorithm should minimize the pixel energy outside the ROI.

$$\mathcal{C}_1 = \{g(x,y) | g(x,y) = 0 \quad \text{for} \quad (x,y) \notin ROI\} \tag{5.6}$$

where the projection operator is given by

$$P_1 g = \begin{cases} g & \text{if } (x,y) \in ROI \\ 0 & \text{otherwise} \end{cases} \tag{5.7}$$

(2) Consistency constraint: A specified region in the k-space contains spatial frequency data interpolated from the available acquired data. Therefore, error between the interpolated values and the k-space values of the image reconstructed at each iteration, should be minimized.

$$\mathcal{C}_2 = \{g(x,y) | G(k_x,k_y) = S(k_x,k_y) \quad \text{for} \quad (k_x,k_y) \in R_o\} \tag{5.8}$$

where $G(k_x,k_y)$ is the Fourier transform of $g(x,y)$, $S(k_x,k_y)$ is the k-space obtained by the application of the algorithm in Section 5.4 and R_o represents all the non-zero k-space grid points in $S(k_x,k_y)$. The projection operator is given by

$$P_2 g = \mathcal{F}^{-1} \begin{cases} S(k_x,k_y) & \text{if } (k_x,k_y) \in R_o \\ G(k_x,k_y) & \text{otherwise} \end{cases} \tag{5.9}$$

(3) Maximum pixel sum and positivity constraint: The total pixel sum of the reconstructed image should be equal to a known value A, where $A \approx S'(0,0)$. It is also known that all the pixel values should be positive and real values.

$$\mathcal{C}_3 = \{g(x,y) | g(x,y) = \frac{A}{\epsilon} g(x,y) \quad \text{if} \quad Re(g) > 0\} \tag{5.10}$$

where $Re(g)$ is the real part of $g(x,y)$ and $\epsilon = \sum_{x=0}^{N-1} \sum_{y=0}^{N-1} g(x,y)$.

The projection operator is given by

$$P_3 g = \begin{cases} 0 & \text{if } Re(g) \leq 0 \\ \frac{A}{\epsilon} Re(g) & \text{if } Re(g) > 0 \end{cases} \tag{5.11}$$

(4) Amplitude constraint: The amplitudes of all $g(x, y)$ must lie within a prescribed closed interval $[I_{min}, I_{max}]$.

$$\mathcal{C}_4 = \{g(x, y) | I_{min} \leq g(x, y) \leq I_{max}\} \tag{5.12}$$

The projection operator is given by

$$P_4 g = \begin{cases} I_{min} & \text{if } g(x, y) < I_{min} \\ I_{max} & \text{if } g(x, y) > I_{max} \\ g(x, y) & \text{if } I_{min} \leq g(x, y) \leq I_{max} \end{cases} \tag{5.13}$$

where $I_{min} = 0$ and $I_{max} = 255$ for general grey-scale images.

Since the POCS method does not converge to a unique solution, the resulting reconstructed image may diverge from the desired solution while converging simultaneously to all the given constraints. Therefore, a regulatory indicator of closeness to the solution is required. The known information on the rotational motion parameters can be used for this purpose. It is possible to estimate the image with artifacts, from the solution at the i^{th} iteration $g_i(x, y)$, using Equation (5.14).

$$\hat{m}(x, y) = \mathcal{F}^{-1} \left[\sum_{x=0}^{N-1} \sum_{y=0}^{N-1} g_i(\bar{x}, \bar{y}) e^{-i \frac{2\pi}{N} (x k_x + y k_y)} \right] \tag{5.14}$$

where $\bar{x} = x \cos \theta_r(k_y) - y \sin \theta_r(k_y)$ and $\bar{y} = x \sin \theta_r(k_y) + y \cos \theta_r(k_y)$. $\theta_r(k_y)$ is the angle of rotation at the ${k_y}^{th}$ phase encode. $\mathcal{F}^{-1}$ represents the inverse Fourier transform. The estimated image with artifacts is $\hat{m}(x, y)$.

The image with artifacts, $m'(x, y)$, can be directly computed using inverse Fourier transform on the acquired data. The regulatory error metric can then be defined based on the difference between the estimated and computed images with artifacts, as given in Equation (5.15). More specifically, the objective is to seek

the image $g_i(x, y)$, that minimizes the difference between $\hat{m}(x, y)$ and $m'(x, y)$. Thus,

$$E = \frac{\sum_{x=0}^{N-1} \sum_{y=0}^{N-1} \|\hat{m}(x, y) - m'(x, y)\|}{\sum_{x=0}^{N-1} \sum_{y=0}^{N-1} \|m'(x, y)\|} \times 100\% \tag{5.15}$$

However, the computation of E requires prior calculation of $\hat{m}(x, y)$, which is computationally intensive. Therefore, a large proportion of the processing time has to be allocated for the calculation of E at each iteration.

In the event of non-intersecting convex sets, it will be clearly shown later in the simulation results (Section 5.6 Figures 5.10, 5.11 and 5.13) that the energy outside the ROI (denoted by E_1) *cannot be used* to indicate the point of termination of iterations. It will be shown that in such an event, the energy outside ROI (i.e. E_1) continues to decrease monotonically, however the mean squared error (MSE) of the reconstructed image goes through a single minimum value. The variation of the regulatory error metric (i.e. E) is equivalent to the variation of MSE, which also goes through a single minimum. Therefore, contrary to the popular belief, the energy outside ROI cannot be used as a substitute for MSE to indicate the quality of the reconstructed image, when dealing with non-intersecting and unreliable sets. If the decision to terminate the iterations have to be governed by the energy outside ROI (i.e. E_1), it is essential to change the behaviour of MSE during the POCS iterations, so that the minima is avoided and a monotonically decreasing characteristic for MSE is achieved. If such a behaviour for MSE is achieved, the termination of POCS iterations can be the conventional termination condition which is,

$$(E_1)_n - (E_1)_{n-1} < \epsilon \tag{5.16}$$

where $(E_1)_n$ is the energy outside ROI at the n^{th} iteration, and ϵ is a small predefined number. This is targeted in Chapter 6 using a fuzzy POCS algorithm.

However, if conventional POCS is used (instead of fuzzy POCS), the MSE going through a minimum *cannot* be avoided. Therefore, in this chapter, the following termination condition is used to terminate the iterations.

$$E_{n+1} - E_n \geq 0 \tag{5.17}$$

where E_n is the regulatory error metric given in Equation 5.15 at the n^{th} iteration. The resulting image from the n^{th} iteration is therefore considered as the final solution (i.e. not the result of the $(n+1)^{th}$ iteration), if the above condition is satisfied.

5.6 Simulation Results

Several simulation experiments were conducted in order to test the effectiveness of the proposed assignment of weights. The Shepp and Logan phantom [121] was used because of the ease of comparison to the bilinear superposition algorithm [78].

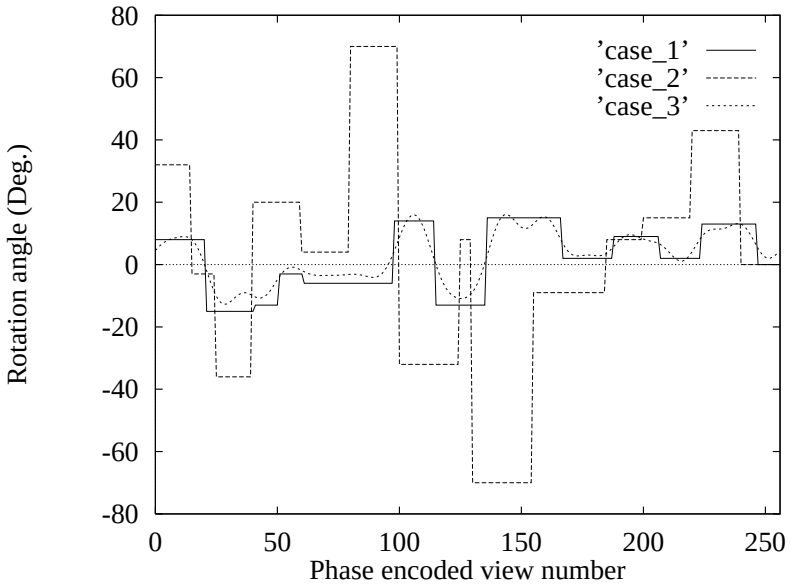

Figure 5.3: Rotational motion parameters for each phase encode.

The rotational motion artifact was simulated by rotating the phantom by an angle θ prior to obtaining the spatial frequency information for each view. The corrupted N samples of data for the k_y^{th} view is given by

$$S'(k_x, k_y) = \sum_{x=0}^{N-1} \sum_{y=0}^{N-1} m(x\cos\theta_r - y\sin\theta_r, x\sin\theta_r + y\cos\theta_r) e^{-i\frac{2\pi}{N}(xk_x + yk_y)} \quad (5.18)$$

where k_x is the sample number in the frequency encoded direction, $m(x, y)$ is the original Shepp and Logan phantom and θ is the angle of rotation for the ${k_y}^{th}$ view.

Figure 5.3 shows the view numbers and corresponding angles of rotation for three different cases studied. The rotations involved stepping, as well as continuous motion. The maximum angular span was $\pm 15^o$ for case 1 and case 3, and $\pm 70^o$ for case 2. The image with artifacts, for case 1 is shown in Figure 5.4(b). A relative measure on the quality of the reconstructed image was obtained using the mean squared error (MSE), which was previously defined in Equation 4.8.

(a) *(b)*

Figure 5.4: *(a)* Shepp and Logan phantom *(b)* Computed image with artifacts(MSE=1942.531).

The following weighted averaging methods were examined, using 3 different sets of simulated MR data (i.e. cases 1 to 3).

Type 1 - Amplitude based weighted averaging : The higher the amplitude of the overlapping sample, the larger the assigned weight. Therefore, the weight w_r

related to the r^{th} sample S_r is given by,

$$w_r = |S_r| \tag{5.19}$$

Type 2 - Rotation angle-based weighted averaging : The smaller the associated rotation angle of the overlapping sample, the larger the assigned weight. If the rotation angle associated with the r^{th} sample is θ_r, the weight is given by

$$w_r = \frac{1}{\theta_r} \tag{5.20}$$

Type 3 - Grid offset based weighted averaging : The smaller the grid offset "g" (see Figure 5.2(b)) of the overlapping sample, the larger the assigned weight. The grid offset distance is given by

$$g_r = \sqrt{(k_{yo}\cos\theta + k_{xo}\sin\theta - k_y)^2 + (k_{xo}\cos\theta - k_{yo}\sin\theta - k_x)^2} \tag{5.21}$$

where (k_{xo}, k_{yo}) are the coordinates of the grid point, k_y is the phase encoded view number and k_x is the sample number. Therefore, the weight is given by

$$w_r = \frac{1}{g_r} \tag{5.22}$$

Type 4 - Equal weight averaging : All the competing samples are assigned the same weight, where the associated weight for any sample is given by

$$w_r = 1 \tag{5.23}$$

Type 5 - Proposed weighted averaging scheme : based on the value of "d" (see Figure 5.2(b)). The weight assignment is as given by Equation 5.5.

The following error metric was used for comparing the accuracy of the corrected k-spaces using different weighted averaging methods.

$$E_{ksp} = \frac{1}{M}\left[\sum_{k_x}\sum_{k_y}\left|{S_r}^R(k_x,k_y) - {S_r}^{(O)}(k_x,k_y)\right| + \left|{S_i}^R(k_x,k_y) - {S_i}^{(O)}(k_x,k_y)\right|\right] \tag{5.24}$$

$\forall (k_x, k_y) \in R_o$.

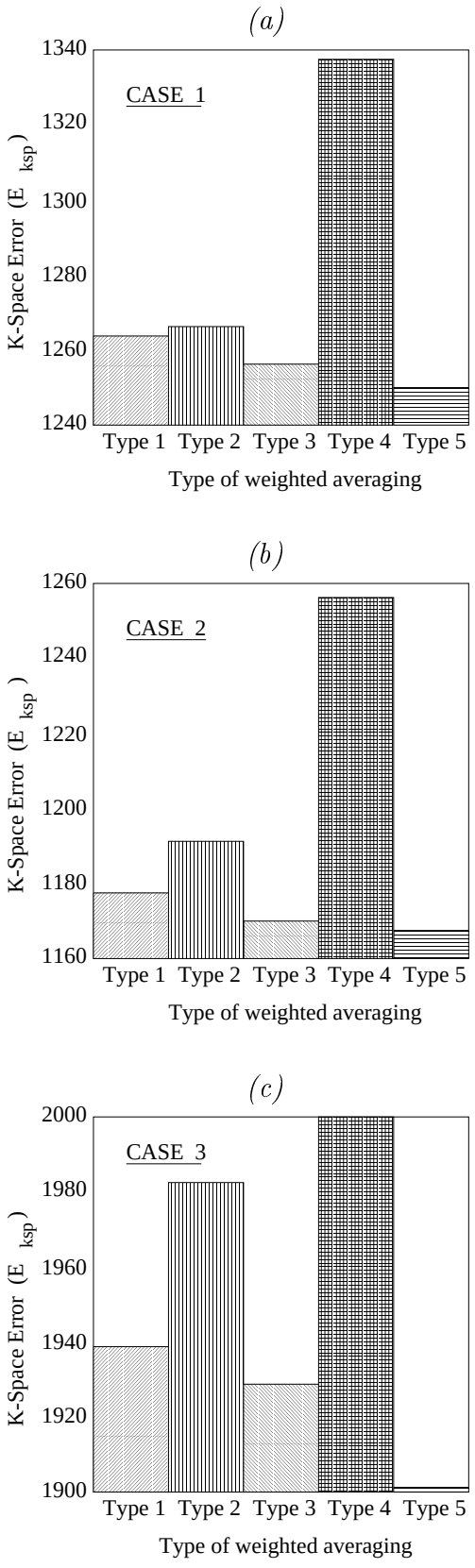

Figure 5.5: K-Space error for weighted averaging schemes used: *(a)* case 1; *(b)* case 2; *(c)* case 3.

In Equation 5.24, R_o is the set of all overlapping grid points, and M is the total number of elements in R_o. S^R is the corrected k-space whereas S^O is the uncorrupted original k-space. S_r and S_i represent the real and imaginary parts respectively.

Figure 5.5 presents the performance of weight assignment methods examined. It is clear that the proposed scheme (i.e. type 5) produce the least k-space error.

(a) *(b)*

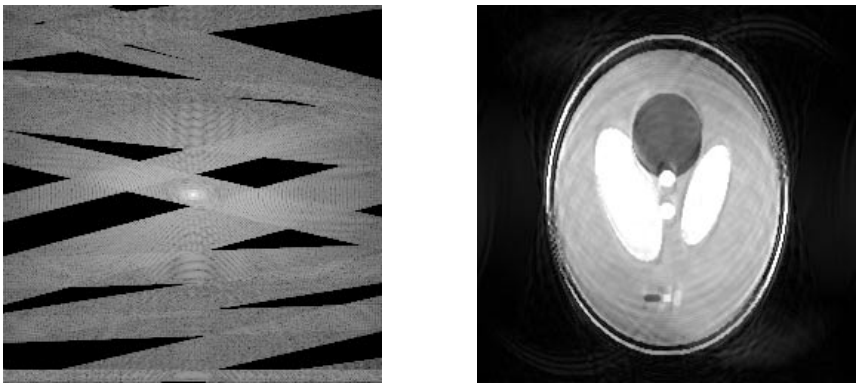

Figure 5.6: *(a)* Corrected k-space using BSA. Log magnitude of the spatial frequency components normalized to 0-255 *(b)* Reconstructed image using BSA (MSE=541.434).

(a) *(b)*

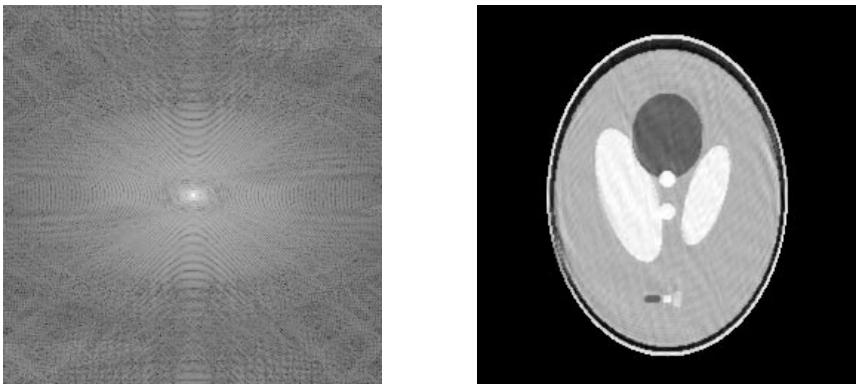

Figure 5.7: *(a)* Corrected k-space using the proposed iterative algorithm. Log magnitude of the spatial frequency components normalized to 0-255 *(b)* Reconstructed image after 10 iterations (MSE=111.595).

For Case 1, the bilinear superposition algorithm (BSA) [78] was used first to reconstruct the image for comparison purposes. The resulting corrected k-space

and the resultant image are shown in Figures 5.6(a) and 5.6(b) respectively. The data overlap and void regions can be clearly seen in Figure 5.6(a). The improved iterative algorithm was then used to reconstruct the image from the corrupted data. The result after 10 iterations is shown in Figure 5.7(b) and the corresponding corrected k-space in Figure 5.7(a). No regions of data overlap, or regions of data void are visible in Figure 5.7(a).

(a)

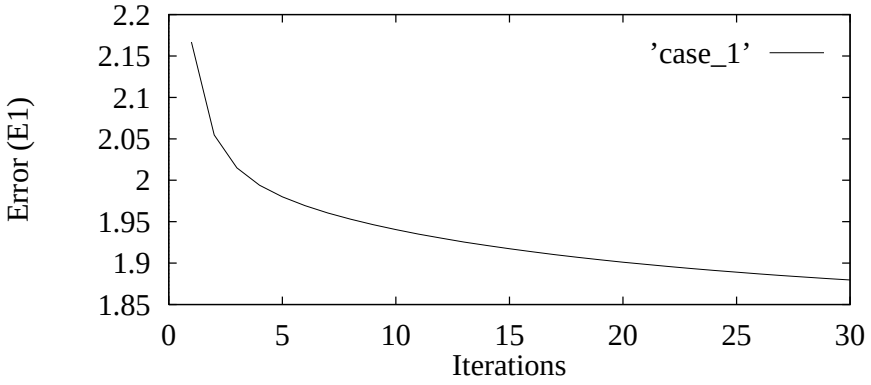

(b)

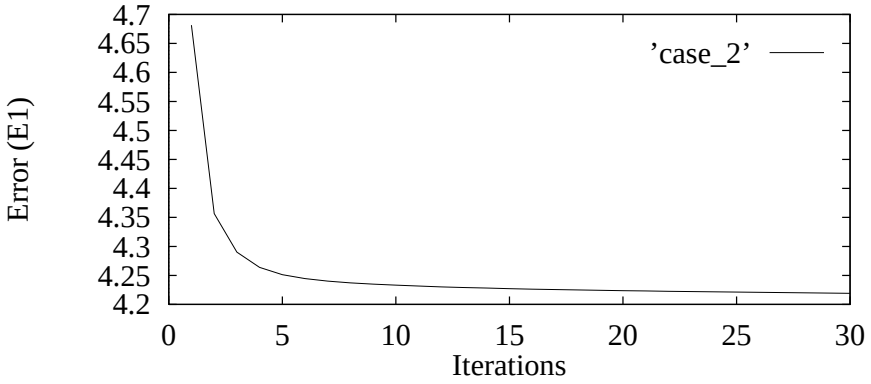

Figure 5.8: Variation of the error outside the ROI (E_1) for 30 iterations: (a) Case 1; (b) Case 2.

To illustrate the convergence of the algorithm, the residual error outside the region of interest after each iteration, was used as the error metric, which is given by

$$E_1 = \frac{1}{N^2} \sum_{x=0}^{N} \sum_{y=0}^{N} |g_i(x,y)|^2 \quad \text{for} \quad (x,y) \notin ROI \tag{5.25}$$

where $g_i(x, y)$ is the reconstructed image, before the application of the projection operator corresponding to the convex set $\mathcal{C}_1$, at the i^{th} iteration. If the algorithm is converging, this error should be reduced after each iteration, indicating convergence to the given convex set, as observed in Figure 5.8.

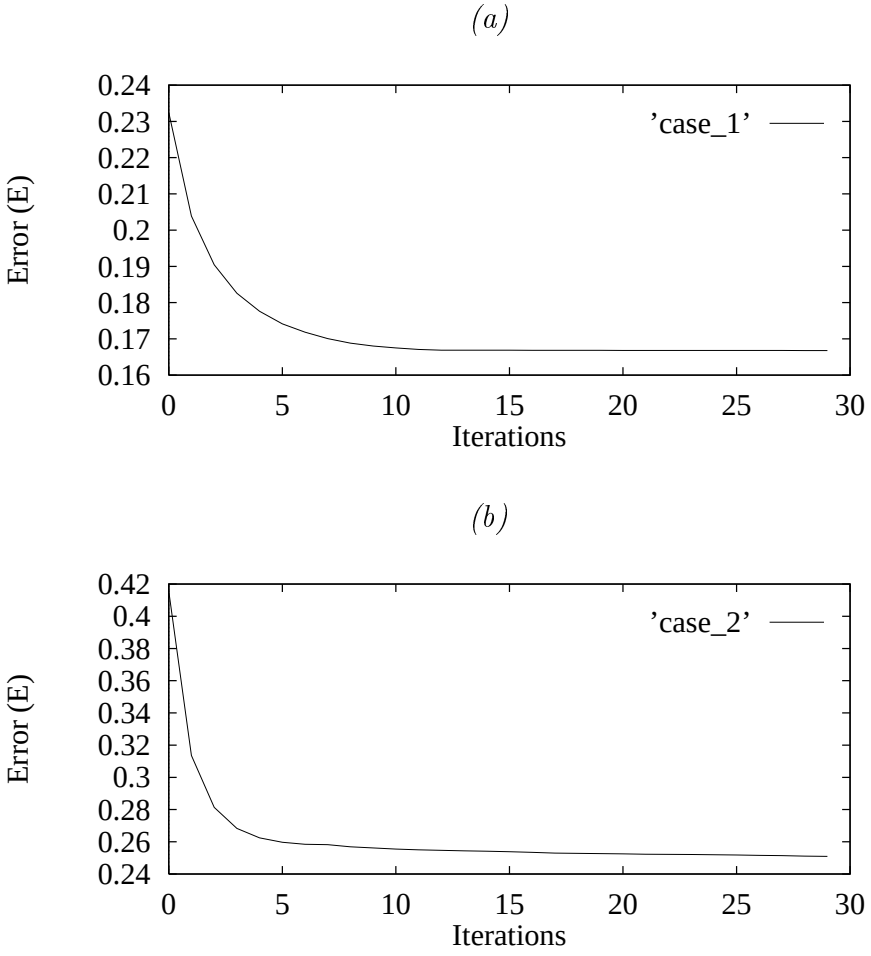

Figure 5.9: Variation of the regulatory error metric (E) for 30 iterations: (a) Case 1; (b) Case 2.

Figure 5.9 shows the variation of regulatory error metric (E) as given in Equation 5.15. It should be noted that any solution in the intersection set $\mathcal{C}_o$ is consistent with the given constraints and therefore a feasible solution. In general, there are many feasible solutions, if the set $\mathcal{C}_o$ contains more than a single element. Therefore, the solution may diverge from the expected result while converging to the intersection set $\mathcal{C}_o$, since the algorithm may be converging to another possible solution in $\mathcal{C}_o$, instead of the expected solution. The number of

elements in $\mathcal{C}_o$ can be restricted by introducing additional *a priori* information in order to force the algorithm to converge towards the expected solution. However, in practice, available *a priori* information is limited. Therefore, expectation of a unique solution is unrealistic. Hence, the regulatory error metric is introduced, which indicates the closest possible reconstructed image to the expected result, at its minimum value. The iterations are terminated when E reaches its minimum.

(a)

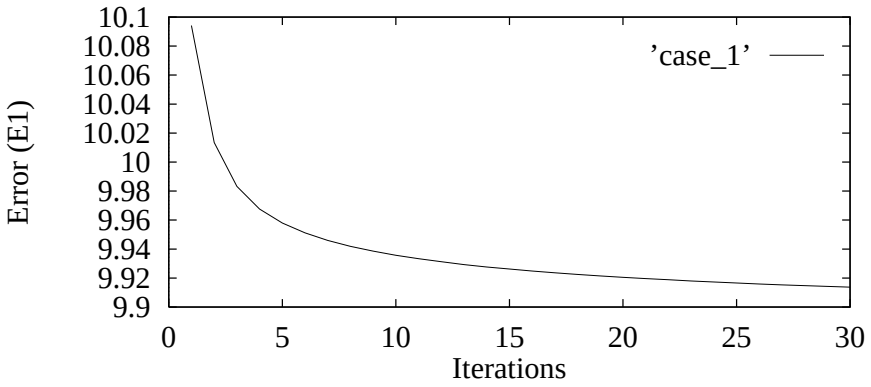

(b)

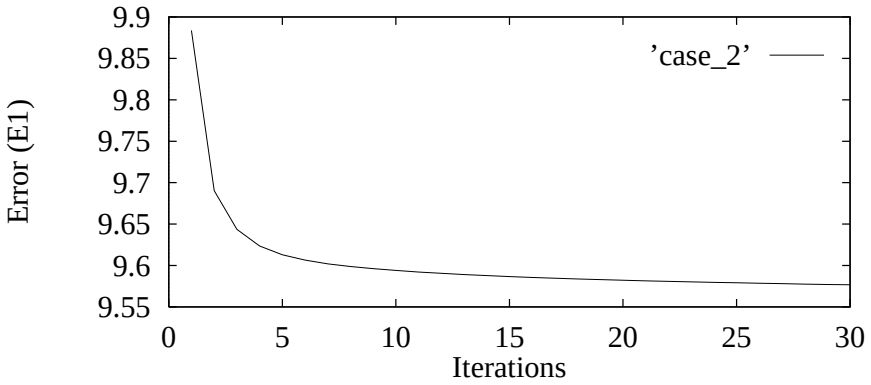

Figure 5.10: Variation of the error outside the ROI (E_1) for noisy data (SNR = 10 dB): (a) Case 1; (b) Case 2.

In certain circumstances, the expected image may not belong to one or more convex sets. For example, the set $\mathcal{C}_1$ is violated when there is severe noise in the acquired data. $\mathcal{C}_2$ may be violated due to noise and interpolation errors. Therefore, the proposed algorithm may not be able to converge to the original image.

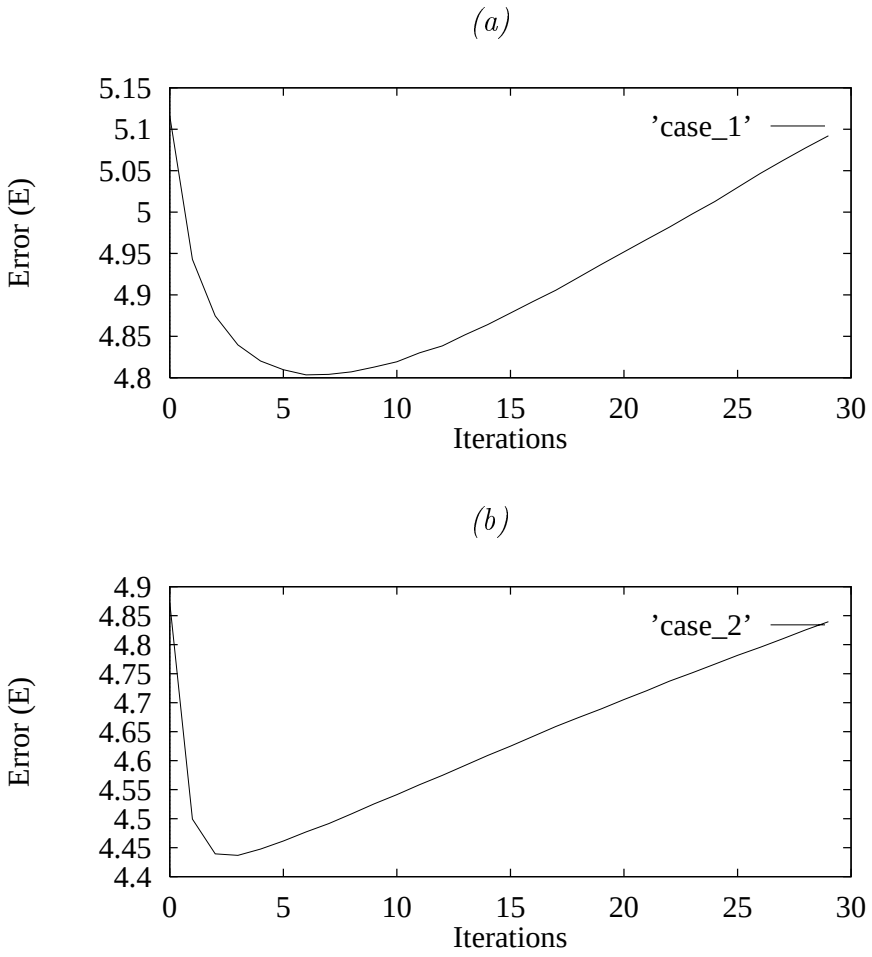

Figure 5.11: Variation of the regulatory error metric (E) for noisy data (SNR = 10 dB): (a) Case 1; (b) Case 2.

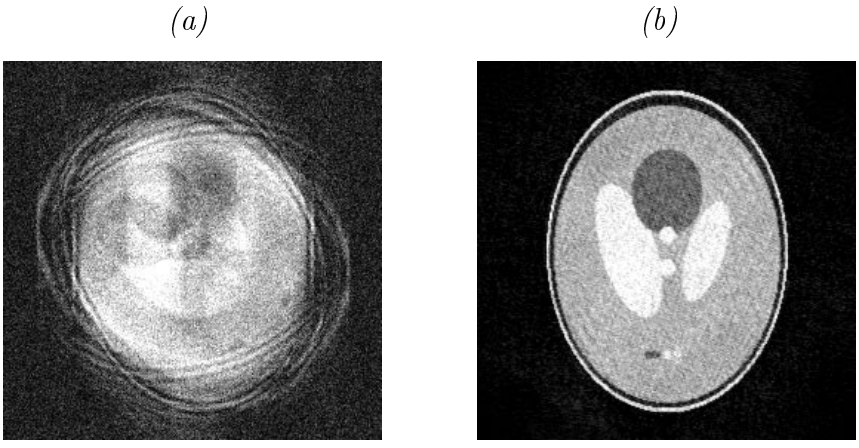

Figure 5.12: *(a)* Image with artifacts, for case 2 at SNR = 10 dB (MSE=3180.528) *(b)* Reconstructed image using the proposed algorithm at SNR = 10 dB (MSE=306.889), after 3 iterations.

However, it can be shown that the proposed algorithm is capable of improving the image quality compared to the bilinear superposition algorithm. In such a situation, E goes through a single minimum, although E_1 continues to decrease. The optimal image can be obtained by terminating the iterations at the minimum value of E.

Convergence properties of the algorithm is examined subject to noisy data at 10 dB signal-to-noise ratio (SNR). The results are shown in Figures 5.10, 5.11 and 5.12.

(a)

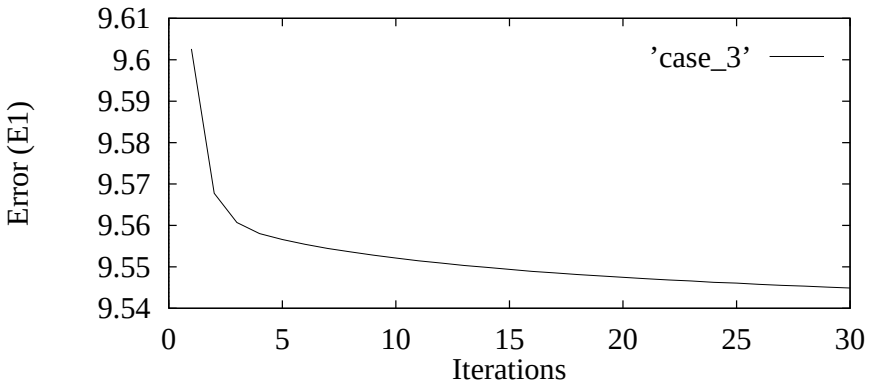

(b)

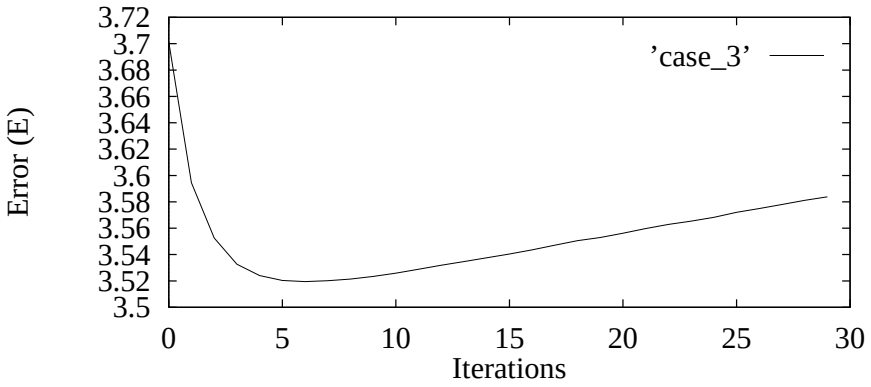

Figure 5.13: Variation of E_1 and E for case 3, with $\pm 1^o$ errors in motion parameter estimation: (a) E_1; (b) E.

The data set in Case 3 is used to test the algorithm for continuous motion with $\pm 1^o$ errors in motion parameter estimations. Figure 5.13 shows the results

obtained. It can be observed that E_1 and E exhibit a similar type of behavior as with noisy data. Errors in parameter estimations forces convex set $\mathcal{C}_2$ to be violated, and hence the original object no longer is contained within $\mathcal{C}_2$. However, the algorithm converges towards the solution for a finite number of iterations. The algorithm is terminated when E reaches its minimum.

(a) *(b)*

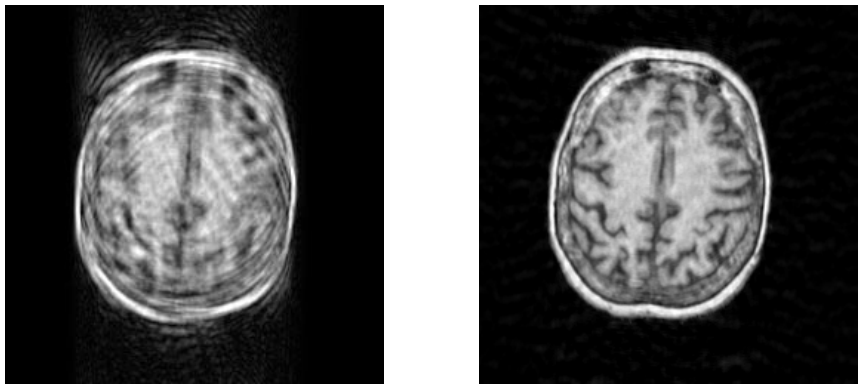

Figure 5.14: *(a)* Image with artifacts, for an axial head MR image (MSE=1147.2) *(b)* Reconstructed image using the proposed algorithm (MSE=106.7), after 5 iterations.

(a) *(b)*

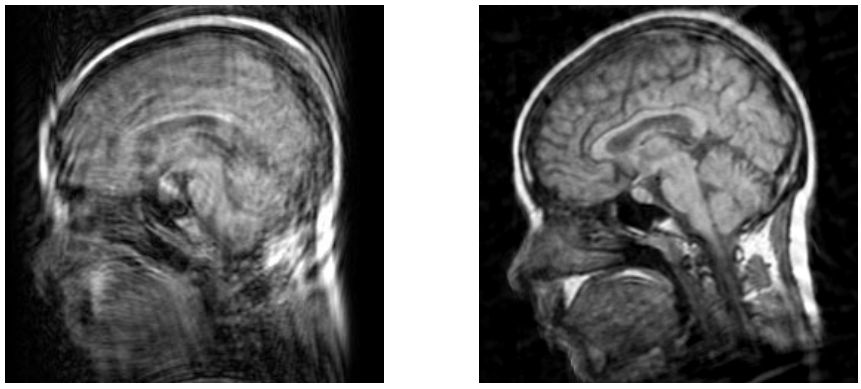

Figure 5.15: *(a)* Image with artifacts, for a sagittal head slice MR image (MSE=2640.1) *(b)* Reconstructed image using the proposed algorithm (MSE=428.4), after 5 iterations.

In order to examine the performance of the proposed algorithm on real MR spin echo images, the data sets associated with axial and sagittal head slices were used, with the rotation angles estimated in Chapter 4 (see Figure 4.11). The

reconstructed image and the image with artifacts (for comparison) are shown in Figures 5.14 and Figures 5.15 for axial and sagittal head slices respectively.

The sensitivity to the accuracy of the selected ROI was investigated using 10% and 30% increases in the area of the ROI. The data set in Case 1 was used. The variation of E with the iterations is shown in Figure 5.16. It can be observed that with larger estimates for the area of ROI, the initial convergence rate significantly decreases.

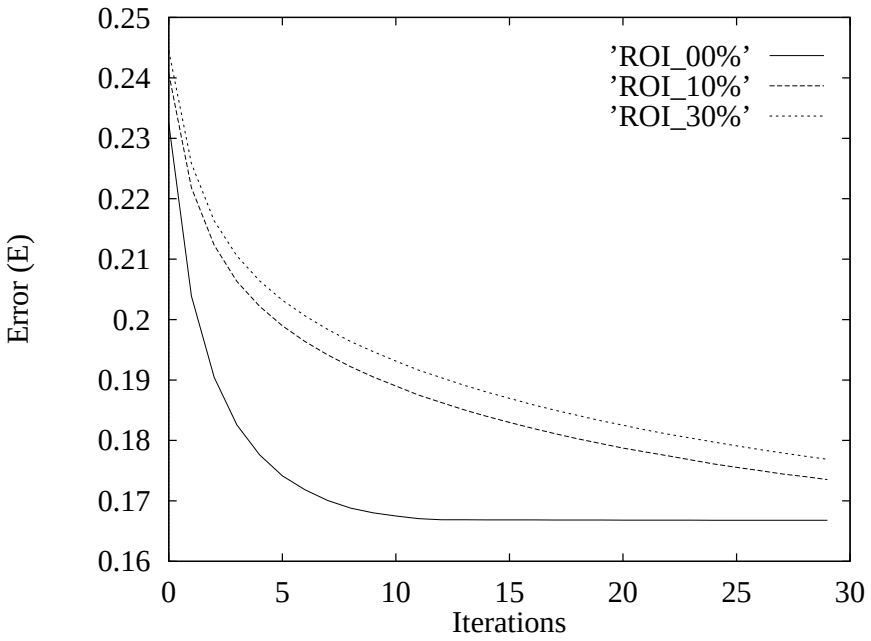

Figure 5.16: Variation of E for case 1, with 0%, 10% and 30% increases in the area of the ROI.

Each iteration of the algorithm takes less than 8 seconds to complete, on a Sun SPARC 2 station, excluding the computation of E. Since the interpolation takes up the bulk of the computational time, the additional computational time required to obtain approximately 80% improvement in MSE, compared to the bilinear superposition algorithm [78], is at most 25%.

5.7 Summary

In this chapter, an improved algorithm for the suppression of in-plane rotational motion artifacts in 2DFT MR images has been presented. The major differences between this algorithm and other previous work [78] [80] are, optimal management of redundant data, by using a weighted averaging scheme and iterative estimation of data in unfilled regions of the k-space, by the use of POCS. The simulation results indicate that the algorithm effectively improves the quality of the final image. The iterative algorithm is also shown to be robust against noisy data and small errors in rotation angles. This algorithm is particularly suited for artifact correction of MR signals subjected to large angle rotations.